Full Three-Dimensional Motion Characterization of a Gimballed Electrostatic Microactuator

Christian Rembe, Lilac Muller, Richard S. Muller, Roger T. Howe
Berkeley Sensor&Actuator Center, University of California at Berkeley
497 Cory Hall; Berkeley, CA 94720
510-642-6256; fax: 510-643-6637; e-mail: rembe@eecs.berkeley.edu

PURPOSE

Advanced testing methods for the dynamics of microdevices are necessary to develop reliable marketable microelectromechanical systems (MEMS). The main purpose for MEMS testing is to provide feedback to the design-and-simulation process in an engineering development effort. This feedback should include device behavior, system parameters, and material properties. An essential part of a more effective microdevice development is high-speed visualization of the dynamics of MEMS structures. We have developed and employed a full three-dimensional-motion-characterization system for MEMS to observe the response of a gimballed microactuator, a multi-degree-of-freedom microdevice. [*Keywords*: MEMS testing, interferometry, stroboscopy, image processing, hard-disk drives]

INTRODUCTION

MEMS are typically characterized by comparing the system output with a defined input function. For example, in the case of an electrostatic actuator with an integrated sensor, the input driving voltage is compared with the signal of the capacitive sensor that corresponds to the actuator displacement. Static characteristics as well as frequency-response behavior can be investigated with these methods, but it does not provide knowledge about any failure mechanisms of the microactuators. The dynamics of microstructures have to be studied using optical-measurement techniques for this information [1,2]. In the example of an electrostatic actuator, failure modes might result from excitation of mechanical modes that interfere with the pure deflection motion.

In this paper we present a new microscopic stroboscopic interferometer system that allows the full three-dimensional-motion measurement of rapidly moving microstructures. The interaction of mechanical modes that move in plane with the out-of-plane-deflection modes can be investigated with our system. The system extracts in-plane, rigid-body motion by employing digital-image processing with a resolution better than 5nm. In addition, the system can measure out-of-plane-deflection maps at defined time points of a periodical motion using interferometric techniques. Out-of-plane displacement can be measured with a resolution better than 1nm. In-plane and out-of-plane motions are measured together in a single experiment and with high precision. This new system is capable of measuring periodic or reproducible transient processes.

Extraction of MEMS in-plane, rigid-body motion from a pseudo-cinematographic image sequence has been reported in [3,4]. We use a similar technique for the in-plane-motion determination. The algorithm reported previously is capable of extracting in-plane displacements between two images that correspond to less than a digital pixel. The algorithm presented in this paper extracts reliable in-plane deflections over several pixels with sub-pixel resolution. The measurement of out-of-plane deflections using a stroboscopic interferometer system has been presented by us in [5,6]. Our new system combines the out-of-plane deflection measurement with a new in-plane motion-measurement feature. We demonstrate the use of this three-dimensional motion-characterization method by studying the response of a micromachined gimballed actuator developed for a hard-disk-drive application.

The measurement of pure out-of-plane deflections can also be performed with a commercially available Laser-Doppler-Scanning Vibrometer from Polytec PI [7,8]. This system measures the velocity of a moving surface via the Doppler frequency shift of a reflected Laser beam. The displacement at a single spot of the surface under investigation is computed by integrating the velocity measurement. However, the vibrometer can only measure one-dimensional motion. Full three-dimensional, rigid-body motion can be investigated with a commercially available Networked Probe Station from Umech [9]. This system is a stroboscopic microscope. A periodic motion of a microstructure, which is imaged with a microscope on a CCD camera, is frozen with a strobed light. Digital image processing is used to calculate the sub-pixel-in-plane motion. With an additional interferometric technique out-of-plane motion is measured. The Umech system is capable of measuring three-dimensional, rigid-body motion, while the system presented in this paper is capable for the first time of measuring rigid-body, in-plane motion together with out-of-plane-deflection maps of a vibrating device surface in a single experiment.

STROBOSCOPIC MICROSCOPIC INTERFEROMETER

In reference [5] we demonstrate a stroboscopic, computer-controlled, phase-shifting interferometer in high-resolution measurements of out-of-plane motions. In this paper, we describe a system for full three-dimensional motion characterization.

Setup

The schematic of the new three-dimensional Stroboscopic Microscopic Interferometer System (SMIS) is shown in Figure 1.

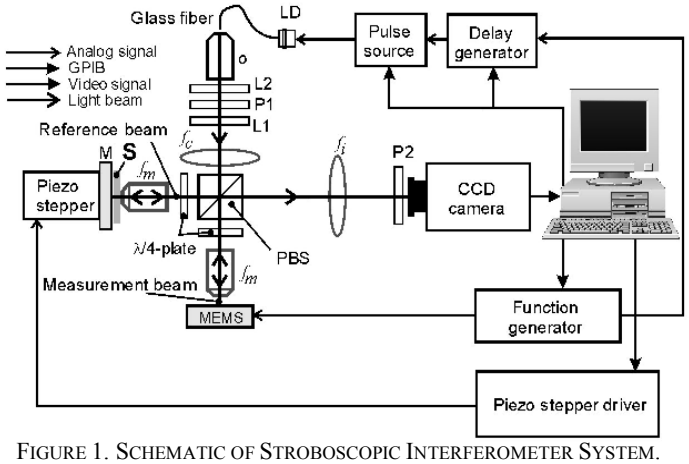

FIGURE 1. SCHEMATIC OF STROBOSCOPIC INTERFEROMETER SYSTEM. THE ABBREVIATIONS USED ARE AS FOLLOWS: L – λ/2- WAVE-PLATE, P – POLARIZER, PBS – POLARIZATION BEAM SPLITTER, f_c – CONDENSER LENS, f_i – IMAGING LENS, AND f_m – MICROSCOPE OBJECTIVE FOR IMAGING, LD – LASER DIODE, M – REFERENCE MIRROR

0-7803-6587-9/01/$10.00 ©2001 IEEE

IEEE 01CH37167. 39th Annual International Reliability Physics Symposium, Orlando, Florida, 2001

The new system can be conveniently used as common light microscope if the light beam that goes to the reference mirror is shadowed with shutter S. Through the stroboscopic visible-light illumination, a set (set 1) of images is taken of the periodic motion without forming an interference pattern. We have developed a new algorithm to extract the in-plane motion from this sequence with a subpixel resolution better than 5nm. After the system has taken a set of images (set 1) without interference fringes the shutter is moved out of the laser beam. Now the system is an interferometer and a set of images (set 2) is taken. The interferometer forms an image of the MEMS device that is crossed by bright and dark fringes that can be interpreted as a contour map of object surface heights. The optical arrangement is that of a Twyman-Green interferometer and is described in detail in [5,6]. To measure the shape of a static specimen or that of a moving specimen, "frozen" by the strobe light, phase-shifting interferometry (PSI) is used.

A five-step PSI algorithm (Hariharan's Algorithm) in which the fringe pattern of a specimen is visualized five times for five different reference-mirror positions is used [6]. The translation data extracted from set 1 are then used to recalculate the in-plane motion from the images of set 2. Finally, the out-of-plane motion is calculated with nm resolution using the five-step-PSI algorithm.

Set 2 contains five images for every single time point where the surface-height map is measured because of the five-step-PSI method. Therefore, to investigate the three-dimensional deflection at 10 time points the systems saves 10 images for the in-plane-motion extraction and 5 times 10 images for the out-of-plane-motion computation. Therefore, full sequence for a measurement at 10 time points contains 60 images.

Analysis Software

The structure of the algorithm, which computes full three-dimensional motion, is presented using analysis software written with MATLAB® (The MathWorks, Inc) and is shown in Figure 2.

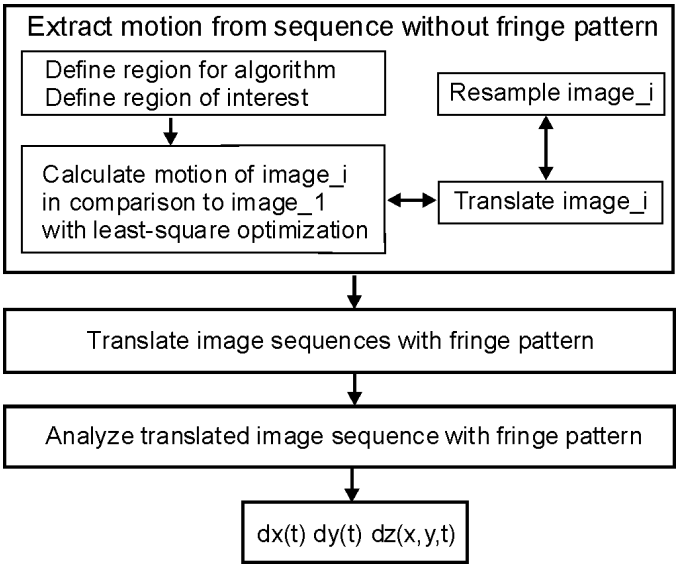

FIGURE 2. STRUCTURE OF THE ANALYSIS SOFTWARE

Algorithm for In-plane-Motion Computation

The user has to specify two regions in the first image of set 1 (image 1) before the in-plane displacement can be calculated. The first region defines the region for the in-plane algorithm. The second region has to be inside the region for the algorithm (ROA) and is termed in Figure 3 as region of interest (ROI). The ROI must be a part of image 1 that shows only the moving structure. The algorithm can only work properly if the structure of the image part in ROI is not deformed somewhere in the ROA of the remaining images of set 1. This is the demand on the definition of ROA that must be ensured by the user. If the ROA is too big, the computation time increases unnecessarily.

In the following, the algorithm for in-plane computation is explained on the example of two images in set 1. The restrictions for the definition of ROA and ROI are specified in Figure 3. For in-plane motion, SMIS can only measure rigid-body motion. The reason for this restriction is that the algorithm can only calculate the in-plane-translational motion of an undeformed structure on the moving specimen in the ROI.

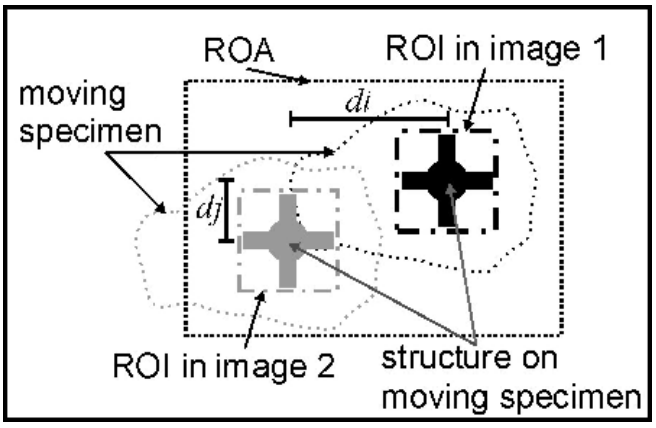

FIGURE 3. DEFINITION AND RESTRICTION OF ROA AND ROI. THE IMAGE SIZE IS DEFINED THROUGH THE RECTANGULAR FRAME.

We number the columns of each picture with i_n and the rows with j_n ($i_n, j_n \in \aleph$). In opposite to the common way row number j_n=1 is at the bottom of the image. Column number i_n=1 is at the first column at the left side as usual. The advantage of this definition is that we can define a coordinate system i and j ($i, j \in \Re$) that coincides for integer values with the numbers of the columns i_n and rows j_n. The displacement di and dj in Figure 3 are computed using digital-image processing. The Progressive-Scan-CCD camera captures 8-bit gray-level images that are saved as TIF-files on the hard disk. They are transformed to matrices using MATLAB®.

In digital-image processing an image is defined as the continuous gray-level-distribution function $I(i,j)$ that one would get with an image sensor having infinite small pixels with the same characteristic as the CCD camera [10]. We use this definition for image in the following.

The sampled-image matrix $\underline{M}$ with components $I_s(i_n,j_n)$ is the TIF-image or MATLAB® matrix and the resampled image $I_r(i,j)$ is the continuous gray-level distribution function that can be calculated from the sampled image by employing the Nyquist-Sampling Theorem. Equation 1 demonstrates this for a sampled image with n columns and m rows.

$$f(i,l)=\sum_{k=1}^{n}\frac{\sin(\pi(k-i))}{\pi(k-i)}I_s(k,j_n)$$
$$I_r(i,j)=\sum_{l=1}^{m}\frac{\sin(\pi(l-j))}{\pi(l-j)}f(i,l)_i \quad (1)$$

The in-plane-motion algorithm calculates the shift *di* and *dj* between image 1 (I_1) and image 2 (I_2) using the least-square-optimization criterion

$$\min(\left\|I_{1,s}(i_n,j_n)-I_{2,r}(i_n-di,j_n-dj)\right\|_2 , \quad (2)$$

where

$$\left\|A(k,l)\right\|_2=\sqrt[2]{\sum_{k,l}A_{k,l}^2}$$

is the L2 norm [11]. The least-square problem in (2) is solved by employing the Nelder-Mead algorithm [12] that is implemented in MATLAB®. This algorithm is very robust in finding the global optimum so that displacements over several pixels are calculated with subpixel resolution. In-plane rotation computation can also easily be implemented with this method using the operation

$$\begin{bmatrix} i_{n,2} \\ j_{n,2} \end{bmatrix}=\begin{bmatrix} \cos\varphi & \sin\varphi \\ -\sin\varphi & \cos\varphi \end{bmatrix}\begin{bmatrix} i_{n,1}-c_i \\ j_{n,1}-c_j \end{bmatrix}+\begin{bmatrix} c_i \\ c_j \end{bmatrix}, \quad (3)$$

with the fulcrum *c* and the rotation angle φ.

However, the direct employment of these methods is not applicable because the computation time for image translation and rotation even for small ROIs is too long (1hour computation time with a Pentium II computer for the data shown in Figure 5 even when linear interpolation is used instead of (1)).

We have developed an algorithm that translates and resamples an image with linear interpolation in one step. The restriction for this algorithm is that rotations in ROI cannot be computed. The algorithm contains a function to shift the columns of a sampled image $\underline{M}$

$$\underline{c}_{i,new}=\underline{c}_{i+1,old} \ , \ \underline{c}_{i,new}=\underline{c}_{i-1,old} \quad (4)$$

to the left or to the right, respectively. Here $\underline{c}_{i,new}$ is the i_n column after the column shift and $\underline{c}_{i\pm1,old}$ the $i_n \pm 1$ column before the shifting. The left column $\underline{c}_1$ of a new right-shifted matrix is set to the null vector. The right column of the matrix, before it is right-shifted, vanishes because the image size stays the same. The opposite is implemented for a shift to the left. The image matrix can be shifted along rows in the same way

$$\underline{r}_{i,new}=\underline{r}_{i+1,old} \ , \ \underline{r}_{i,new}=\underline{r}_{i-1,old} \ , \quad (5)$$

where $\underline{r}_i$ is the i_n row.

Shifts with subpixel resolution are performed with linear combinations of (4) and (5). If we define a matrix $\underline{M}_k$ that is right-shifted about *k* pixels by employing operation (4) a shift to the right about $i \in \Re$, $i \geq 0$ is expressed by

$$\underline{M}_i=(i-k)\underline{M}_k+(k+1-i)\underline{M}_{k+1} \ , \quad (6)$$

when k is the greatest integer which is smaller than *i* ((*i*-*k*)<1). Respectively, a shift to the left about $i \leq 0$ pixel is defined by

$$\underline{M}_i=(i-k)\underline{M}_k+(k-1-i)\underline{M}_{k-1} \ , \quad (7)$$

where *k* is the smallest integer that is greater than *i*. The equations for a shift up or down about $j \in \Re$ pixel are similar to (6) and (7).

For every image the displacement is calculated in respect to the first image. Therefore, no error is accumulated. The calculation time of the data shown in Figure 6 is reduced to 1 minute by formulating the optimization problem (2) with the translation method expressed by (6) and (7).

Algorithm for Out-of-plane-Motion Computation

The in-plane-displacement data between the images is used to calculate the in-plane motion from the interferograms of image set 2 with the image-translation method expressed by (6) and (7). This is necessary to make sure that out-of-plane deflection is computed in respect to points on the device surface. Otherwise the algorithm would compare different points on the surface to calculate deflection, which would be without value. Then we use an algorithm (reported in detail in [3]) summarized as follows.

To measure the shape of a static specimen or that of a moving specimen "frozen" by the strobe light we use phase-shifting interferometry (PSI). We choose a five-step PSI algorithm in which the fringe pattern of a specimen is visualized five times for five different reference-mirror positions. The five-step PSI algorithm calculates a wrapped-phase map and is known as Hariharan's Algorithm. The algorithm calculates the wrapped phase $\phi(i,j)$ from the five intensity amplitudes $I_1(i,j)...I_n(i,j)...I_5(i,j)$ using the formula

$$\phi(i,j)=\arctan\left[\frac{2(I_2(i,j)-I_4(i,j))}{2I_3(i,j)-I_5(i,j)-I_1(i,j)}\right]. \quad (8)$$

Inputs to this algorithm should change phase by approximately $\pi/2$ in each data-acquisition step. The surface under test is assumed to be smooth and continuous; abrupt steps are removed by software.

Our single-wavelength system measures wave-front-phase modulo 2π and, therefore, calculates a "wrapped" phase map from the interferogram sequence. The unwrapped phase map $\varphi(i,j) = \phi(i,j) + 2n(i,j)\pi$ is determined from the wrapped-phase function $\phi(i,j)$ and describes the phase difference of the measurement beam and the reference beam at every pixel of the CCD sensor. The spatially varying integer $n(i,j)$ is present because the optical phase can only be measured modulo 2π in a single-wavelength interferometer.

Finally, the surface-height map *h(i, j)* can be found using

$$h(i,j)=\lambda\cdot\varphi(i,j)/4\pi \ . \quad (9)$$

This procedure is repeated for different strobed-light delays Δt, corresponding to a strobed-light-phase delay $\gamma = 2\pi f_s \Delta t$, with f_s the

strobe frequency. In addition a time unwrapping algorithm is employed to enable the system to measure pure piston motion.

GIMBALLED ELECTROSTATIC MICROACTUATOR

The fully three-dimensional motion characterization of SMIS has been used to study the dynamics of a gimballed electrostatic microactuator [13]. The microactuator, shown in Figure 4, has been designed to increase bandwidth and data-storage capacity of compact hard-disk drives. The microgimbal structure provides pitch and roll compliance between the microactuator and the support system, and thus offers mechanical isolation from external disturbances. These actuators are required to operate in close proximity to the magnetic media. The gap-closing microactuator operates in the yaw direction, co-planar with the spinning hard disk.

Microactuator

Using micromachined actuators for secondary actuation as part of a dual-stage servo control of the read/write-head position has been proposed for increasing data-track density [14]. Secondary actuation, utilizing a microactuator, increases the bandwidth of the system, by allowing faster data-access times. The microactuator developed at the Berkeley Sensor&Actuator Center utilizes an electrostatic drive [15,16]. Figure 4 shows a gimballed actuator with an attached slider. The slider is a rigid, ceramic block that contains the magnetic circuitry that is the read/write head. The slider has an air-bearing surface that improves its aerodynamics as it slides over the disk. The gimballed microactuator is manufactured using a high-aspect ratio dual-thin-film-micromolding process and includes embedded electrical interconnects to the microactuator and the actuated load [15].

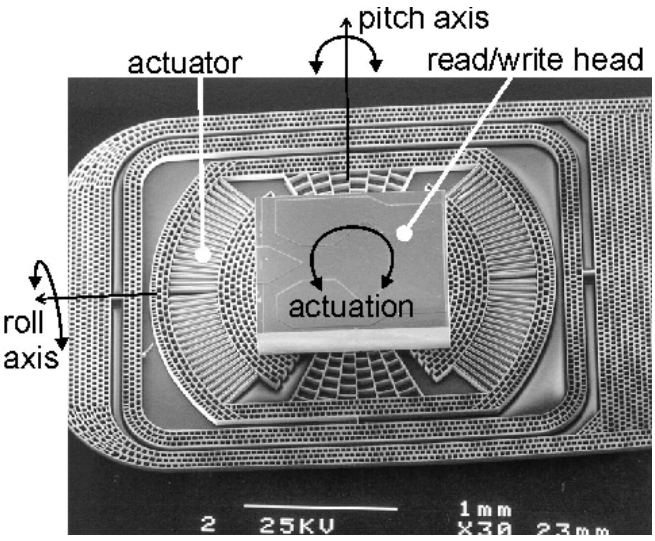

FIGURE 4. SEM PHOTOGRAPH OF GIMBALLED MICROACTUATOR

The force F in an electrostatic gap-closing actuator consisting of two parallel capacitive plates is given by

$$F(V) = \frac{1}{2}\varepsilon V^2 \frac{A}{g^2} \quad , \tag{10}$$

where V is the applied voltage, ε is the permittivity constant in air, A the area of the capacitive plates, and g the variable gap between two plates. Clearly, the force has a nonlinear dependence on the applied voltage. The electrostatic actuator has been designed using a differential-drive-gap-closing configuration, which improves the linearity of the force [16]. A schematic of this configuration for a nominal gap g_0 is shown in Figure 5.

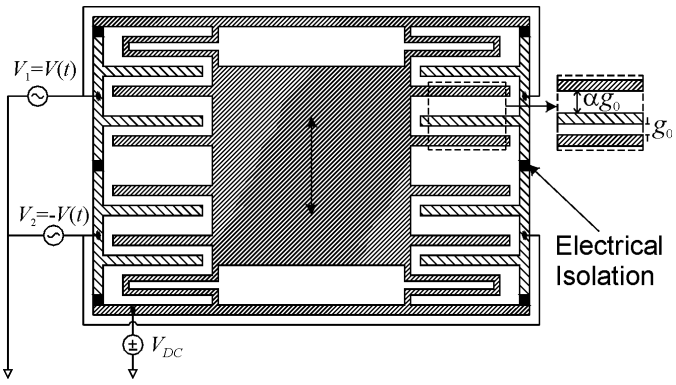

FIGURE 5. SCHEMATIC OF DIFFERENTIAL-GAP-CLOSING DRIVE

The differential-drive configuration has three electrodes. The first electrode is a moving shuttle with a constant applied voltage V_{DC}. A time-dependent-input voltage $V_1=V(t)$ is applied to the first set of stator electrodes and the voltage $V_2=-V(t)$ is applied to the second set, as shown in Figure 5. The improved linearity is due to out-of-phase sinusoid applied to upper and lower sets of electrodes (V_1 and V_2, respectively). Each of the fingers attached to the moving shuttle is acted on simultaneously by two stationary fingers with the distances g_0 and αg_0, respectively.

Theoretical Dynamic Behavior

In the case of rotational actuators, such as the one shown in Figure 4, torques have to be considered instead of forces. With the assumption of small rotation angles θ and a long distance from the capacitive plates to the fulcrum of the actuator, the sum of all applied electrostatic torques yields

$$T_{eg} = \frac{N\varepsilon lhr\left(V - V_{DC}\right)^2}{2}\left(\left(\frac{1}{g_0 - r\theta}\right)^2 - \left(\frac{1}{\alpha g_0 + r\theta}\right)^2\right) - \frac{N\varepsilon lhr\left(V + V_{DC}\right)^2}{2}\left(\left(\frac{1}{g_0 + r\theta}\right)^2 - \left(\frac{1}{\alpha g_0 - r\theta}\right)^2\right) , \tag{11}$$

where N is the number of capacitive plate pairs, l is the overlap length, h is the height of the plates, and r is the distance from the fulcrum to the middle of the capacitive plates. By developing (11) in a Taylor expansion with respect to V and θ the electrostatic torque T_{eg} of the actuator can be approximated.

By assuming a linear mechanical spring with the spring constant k_m, linear viscous damping with the viscous-friction coefficient b the dynamic equation of the electrostatic actuator is derived:

$$J_m\ddot{\theta} + b\dot{\theta} + k_m\theta = T_{eg}\left(\theta, V(t)\right) \quad , \tag{12}$$

where J_m is the moment of inertia of the actuator moving shuttle and the load slider.

By setting all significant terms of the Taylor expansion of (11) in (12) the dynamic equation becomes the structure of a Duffing equation [13]

$$J_m\ddot{\theta} + b\dot{\theta} + \left(k_m - k_e\left(V_{DC}^2\right)\right)\theta - k_D\left(V_{DC}^2\right)\theta^3 = k_i\left(V_{DC}\right)V \quad , \tag{13}$$

with

$$k_m - k_e = k_m - 2N\varepsilon lhr^2 V_{DC}^2\left(\frac{1}{g_0^3} + \frac{1}{\alpha^3 g_0^3}\right), \tag{14}$$

$$k_D\left(V_{DC}^2\right) = 4N\varepsilon lhrV_{DC}^2\left(\frac{1}{g_0^5} - \frac{1}{\alpha^5 g_0^5}\right) \quad ,$$

and with the voltage-amplification factor k_i

$$k_i\left(V_{DC}\right) = 2N\varepsilon lhrV_{DC}\left(\frac{1}{g_0^2} - \frac{1}{\alpha^2 g_0^2}\right) .$$

The influence of the different terms on the dynamic behavior of the micro actuator is investigated experimentally in the next section.

EXPERIMENTAL RESULTS

The gimballed microactuator is driven electrostatically by applying a constant voltage V_{DC} at the rotor of the device and a time-dependent voltage $V(t)$ at the stators. We have studied the influence of the nonlinear terms in (13) on the dynamic behavior of the actuator.

Investigation of in-plane motion

We have studied the in-plane behavior by investigating the device response after a constant voltage V at the stator has been switched off at t = 0µs. Figure 6 shows the mechanical ring down of the actuator deflection $d = r \cdot \theta$ for a voltage V_{DC}=0V at the rotor.

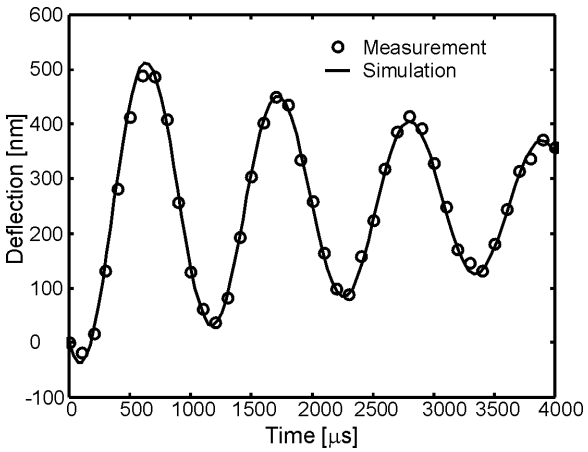

FIGURE 6. RING DOWN OF GIMBALLED ACTUATOR FOR AN INITIAL DEFLECTION OF 255nm (V_{DC}=0V)

In this case the right side of (13) is zero. The ring-down data shown in Figure 5 depend on the resonance frequency $f_0 = 1/2\pi\sqrt{k_m/J_m}$ and the dimensionless damping factor $D = b/2\sqrt{k_m J_m}$. The final deflection and the initial velocity at 0µs also influence the measured ring down and were identified but are not a general system property. The best fit for a second-order system is shown with the measurements in Figure 6. The root-mean-square deviation between the measurements and simulated deflections is 1.69nm. The extracted resonance frequency and damping factor are f_0=921.2Hz and D=0.043, respectively. The moment of inertia was calculated to be J_m = 356pg·m^2 [13] and is slightly higher than the moment of inertia of the slider alone (342pg·m^2). From the measured data, the mechanical spring constant is k_m = 11.5µN·m/rad and the friction coefficient is b = 171pN·m/(s·rad).

For higher values of the rotor voltage the oscillation frequency during the ring down decreases as shown in Figure 7. The voltage at the rotor is V_{DC} = 15V for this experiment. The extracted resonance frequency for this second order system is f_0=801Hz. The reason for the lower resonance frequency is the spring-softening effect expressed through (14) that has a quadratic dependence on V_{DC}.

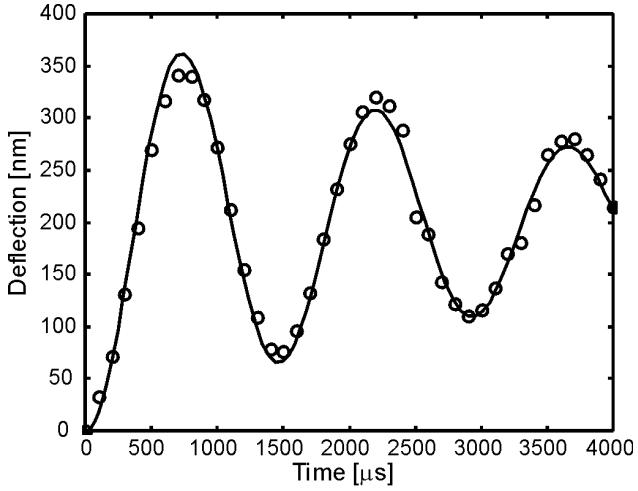

FIGURE 7. RING DOWN OF GIMBALLED ACTUATOR FOR AN INITIAL DEFLECTION OF 199nm (V_{DC}=15V)

In addition, nonlinear behavior due to the Duffing term (term with coefficient k_D in (13)) appears for higher deflections, because this term has a cubic dependence on the deflection and a quadratic dependence on V_{DC}. The experimental result in Figure 8 demonstrates that the oscillation frequency decreases further for higher deflections (940nm instead of 199nm) through the influence of the Duffing term. The extracted resonance frequency is f_0=674Hz for the experiment shown in Figure 8.

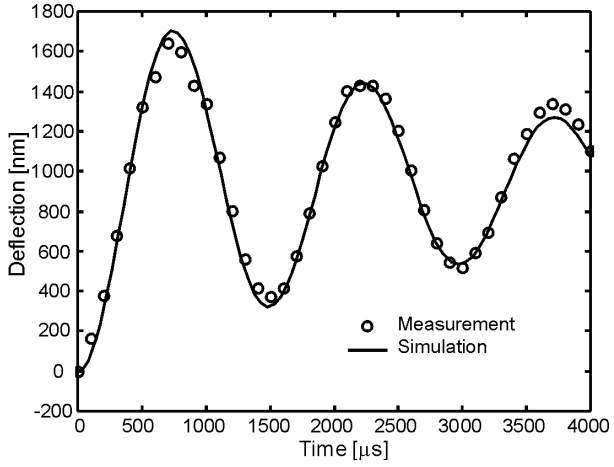

FIGURE 8. RING DOWN OF GIMBALLED ACTUATOR FOR AN INITIAL DEFLECTION OF 940nm (V_{DC}=15V)

Comparison with Laser-Doppler-Vibrometer Measurements

The slider assembled on the microactuator is 0.3mm high. Therefore, it is possible to shine the HeNe-laser beam of the commercial Laser-Doppler-Vibrometer (LDV) OFV 510 from Polytec PI on the side of the slider and measure the in-plane motion this way. The results of the SMIS in-plane-motion experiments are compared to results obtained with the LDV. Results of the experiments with the LDV are shown in Figure 9. We have measured the frequency response of the microactuator between 200 and 1200Hz. The scale of the amplitude (velocity at an edge of the slider) and the frequency are linear. For all experiments the input voltage is a sine wave with an amplitude of 250mV. For V_{DC} =15V the actuator is more sensitive to the input signal and, therefore, the amplitude of the motion is higher.

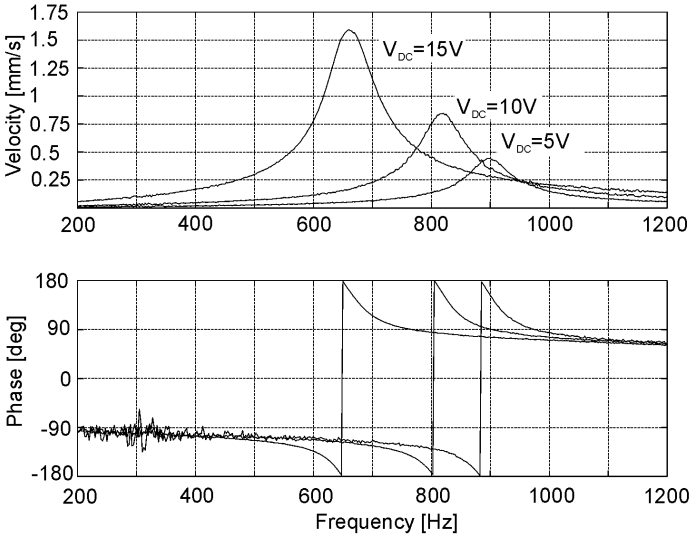

FIGURE 9. FREQUENCY RESPONSE MEASURED WITH LDV

Measurements of resonance frequencies obtained with SMIS for small (<300nm) and large initial deflections (>300nm) and obtained with the LDV for different stator voltages are shown in Figure 10. The resonance frequency for small deflection and large deflections were extracted from ring down experiments. For small deflections the decrease of the resonance frequency results only from the spring-softening term. For higher deflections, the Duffing term has also an influence when the voltage at the stator is V_{DC} = 10V or higher.

Therefore, for V_{DC} = 15V the measured resonance frequency is higher for a small initial deflection (see Figure 7). The amplitude of the motion was high for the LDV measurement and, therefore, the value obtained with the LDV corresponds to the value measured with SMIS at a large initial deflection (see Figure 8). For V_{DC} = 18V the influence of the Duffing term is dominant even for small deflection amplitudes. Therefore, Figure 10 does not show a result obtained with the SMIS at V_{DC} = 18V for a small initial deflection.

The LDV show a good correlation to the results obtained with the SMIS at large initial deflections. As a result of these investigations we are able to estimate limits for the driving signal to avoid influence through the Duffing term. Nonlinear behavior through the Duffing term does appear if the input voltage at the stator is 250mV or higher when the DC voltage at the rotor is higher than 10V.

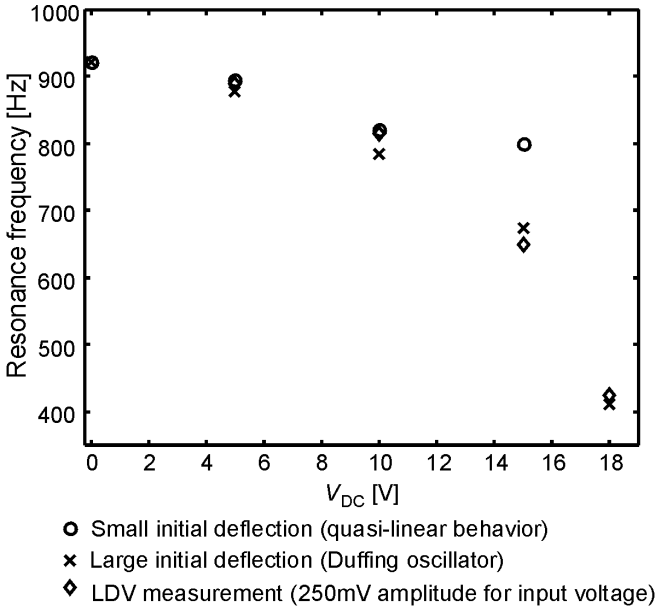

FIGURE 10. SMIS VERSUS LDV RESULTS

Investigation of out-of-plane motion

The torsion springs of the gimbal have been designed to be very stiff in out-of-plane and in-plane directions because the only wanted degree of freedom is rotation, so that the gimbal resonance of vertical displacement should be at higher frequencies as the resonances out-of-plane motion. However, mode coupling could result due to a misalignment between the actuated load and gimballed actuator. Since the load, the read/write head, is much heavier then the micromachined device a slight misalignment could excite an undesired mode if the load main axes of inertia are not parallel or perpendicular to the torque generated by the microactuator. Another cause could be imperfections of the actuator gap-closing structure due to the manufacturing process. The shapes of the etched molds that are used to build the actuator fingers have a limited accuracy and can generate out-of-plane forces. Such effects have to be small to guarantee a reliable dynamic behavior of the device.

No out-of-plane motion was measured at in-plane resonance for different DC voltages (5V, 10V, 15V). Therefore, out-of-plane deflection is smaller than the out-of-plane resolution (5nm) when the device is driven with a harmonic input signal with 0.25V amplitude. However, higher input voltages have to be applied if the device is driven at higher frequencies to achieve sufficient in-plane motion. The highest out-of-plane motion has been empirically found to be 1250Hz by shifting the input frequency with 50Hz steps.

Figure 11 shows the interferograms at 0 and 180 degree phase shift in respect to the input signal with an amplitude of the input voltage of 7.5V (V_{DC}=16V). The height maps corresponding to the interferograms in Figure 11 are presented in Figure 12. In this case the maximal out-of-plane deflection is approximately 100nm. The excited out-of-plane motion consists of pitch and roll motion. We have used a lens combination to take the interferograms in Figure 11 with a low numerical aperture. Therefore, the spatial in-plane resolution of the interferograms is very low (s=10µm) and in-plane motion can not be measured. To demonstrate our combined in-plane and out-of-plane algorithm, we have measured the full three-dimensional motion at one single area on the slider surface for an harmonic input signal with a frequency of 1250Hz, an amplitude of V_m=7.5V ($V(t) = V_m \sin(2\pi f t)$), and a DC voltage V_{DC}=16V. The

area on the device surface that has been investigated is marked in Figure 11.

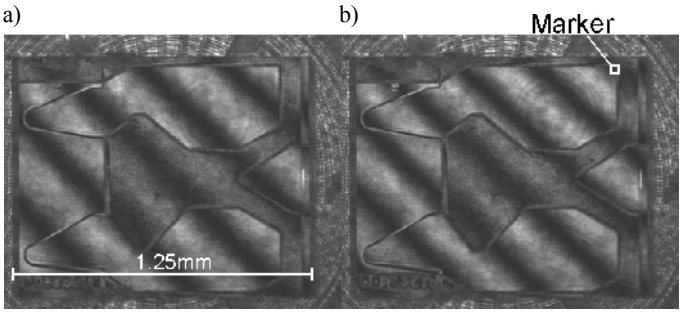

FIGURE 11. INTERFEROGRAMS AT 0 (A) AND π (B) RAD STROBE-PHASE DELAY IN RESPECT TO THE HARMONIC INPUT SIGNAL (1250HZ)

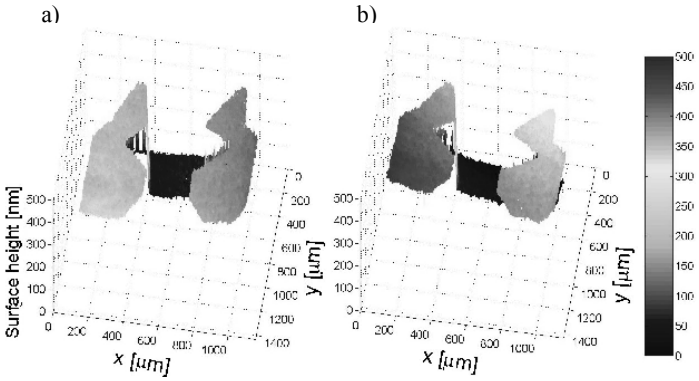

FIGURE 12. CALCULATED HEIGHT MAPS AT 0 (A) AND π (B) RAD STROBE-PHASE DELEAY

Figure 13 shows the freezed images of set 1 at $\gamma = \pi/2$ (a) and $\gamma = 3\pi/2$ rad (b) strobe-phase delay in respect to the input signal.

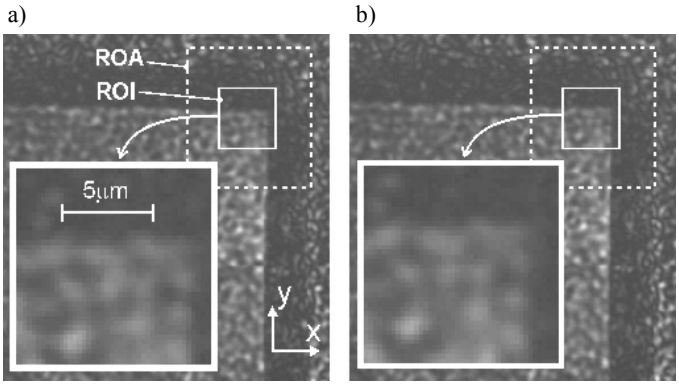

FIGURE 13. IMAGES OF SET 1 AT π /2 (A) AND 3π/2 (B) RAD STROBE-PHASE DELAY IN RESPECT TO THE INPUT SIGNAL. THE REGION OF INTEREST (ROI) IS ZOOMED

The displacement can be clearly seen in the zoomed region of interest. Altogether, 16 strobe-phase delays have been captured. The in-plane algorithm expressed by (6) and (7) is used to calculate the in-plane motion shown in Figure 14.

Then, the in-plane displacement, which is also captured in the images of set 2 is removed by the software using the data shown in Figure 14 and by employing the image-translation method expressed through equations (6) and (7). After the in-plane displacement is removed the surface profile and out-of-plane deflection is calculated with the algorithm expressed by (8) and (9).

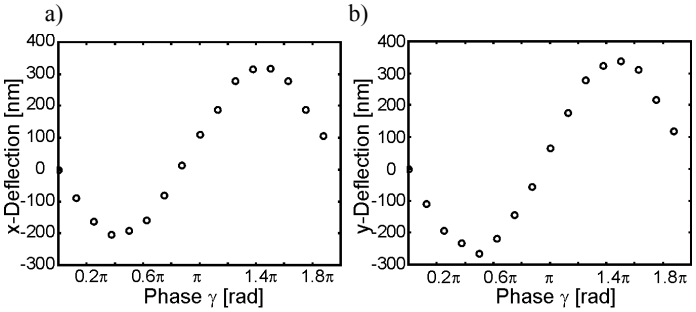

FIGURE 14. IN-PLANE-MOTION AT 1250KHZ, X (A) AND Y (B) DEFLECTION

By performing a least-square optimization a plane is fitted to every height map of the 16 investigated strobe phases. One fit parameter is the z-displacement of the plane that is the out-of-plane deflection. The worst-case-out-of-plane deflection is shown in Figure 15.

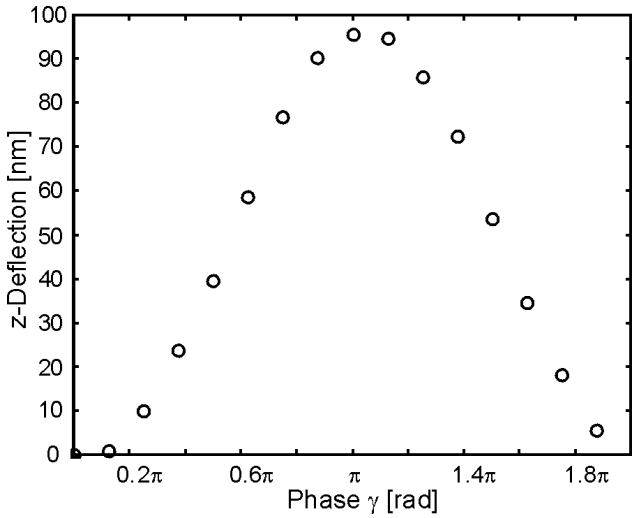

FIGURE 15. OUT-OF-PLANE MOTION AT 1250KHZ

We were only able to excite out-of-plane motion at frequencies higher that 1000Hz and with an very high input-signal amplitude (V_m=7.5V, V_{DC}=16V). It can be guaranteed that for signals with values f<1000Hz, V<1V, and V_{DC}<15V no significant out-of-plane motion is excited and that the slider is capable of sliding smoothly on the air bearing.

SMIS SPECIFICATION

The in-plane-profile resolution is the spatial resolution limited by the numerical aperture of the imaging optic and is approximately 1µm if f_m is a 20x objective. The in-plane-displacement resolution depends on the algorithm and has been investigated with a test image for different initial displacements. A steady object, the slider without any applied voltages, has been captured. No motion should be detected but the measurement in Figure 16 shows a random deflection with maximum amplitude of ±8nm. This experiment shows the noise of the in-plane measurement.

The root-mean-square deviation of this noise measurement is 3.6nm. The noise can result from mechanical vibration or noise of

the camera. The system can detect harmonic motion with an amplitude greater than the root-mean-square deviation (3.6nm), which is the resolution for in-plane motion. Single displacement measurements have a resolution of the maximal noise peak-to-peak amplitude, which is approximately 15nm.

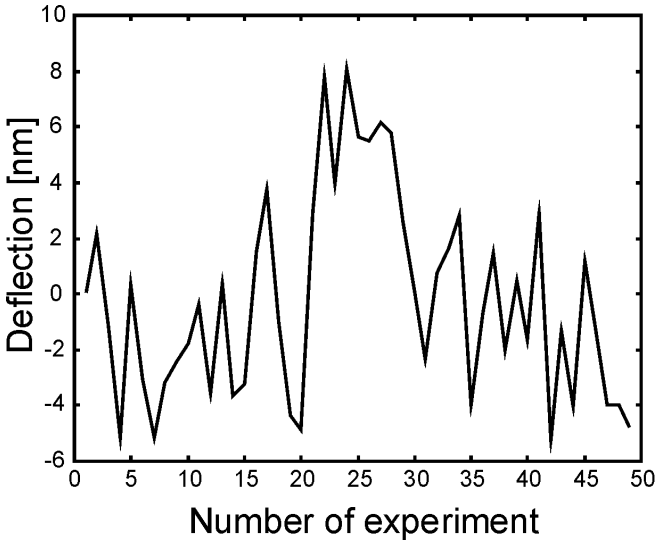

FIGURE 16. TYPICAL IN-PLANE NOISE MEASUREMENT

The resolution of the out-of-plane surface measurement is limited through imperfections in the optical elements and through dust in the optical path. Our improved system keeps the features for out-of-plane measurement that we have reported in [5,6]. The out-of-plane-profile repeatability is less than 5nm and is the limit for displacement resolution. The root-mean-square deviation of out-of-plane noise is approximately 0.7nm and is the limit for the resolution out-of-plane-motion measurements. The out-of-plane-profile resolution is limited through imperfections in the system optics and is approximately 20nm.

CONCLUSIONS AND OUTLOOK

We have presented a MEMS testing system that is capable for the first time of measuring full three-dimensional motions and device-surface profiles of micromachined, multi-degree-of-freedom devices in a single experiment. The new setup is a stroboscopic microscopic interferometer system that saves two sets of images on the computer hard disk. One set is a pseudo-cinematographic-image sequence and is used to compute the in-plane motion. The in-plane-displacement resolution of our new system is less than 5nm. The other set contains interferograms that are used to compute the out-of-plane profile of the specimen for every strobe-light delay that is captured. The resolution for out-of-plane displacement is less than 1nm.

The capability of our system has been demonstrated on the example of a micromachined, electrostatically driven actuator for read/write heads in disk drives. We have investigated linear and nonlinear, in-plane behavior of our device. Nonlinear behavior appears at high input signals and large deflections. Because the slider assembled on the microactuator is 0.3mm high we were able to to shine the HeNe-laser beam of the commercial Laser-Doppler-Vibrometer (LDV) OFV 510 from Polytec PI on the side of the slider and measure the in-plane motion this way. The results obtained with the LDV are in good agreement with the results measured with our new system.

In addition we have measured the worst-case, out-of-plane motion that can be excited. As a result of this investigation we have determined system parameters and limits of operation of the microdevice to guarantee a reliable dynamic behavior.

REFERENCES

[1] P. Krehl et al., High-Speed Visualization, a Powerful Diagnostic Tool for Microactuators – Retrospect and Prospect. *Microsystem Technologies*, Vol. 5, 1999, pp. 113-132.

[2] C. Rembe et al., Analysis of the Dynamics in Microactuators Using High-Speed Cine Photomicrography, to be published in *J. of Microelectromechanical Systems*, Vol. 10, March, 2001.

[3] C.Q. Davis et al., Statistics of Subpixel Registration Algorithms Based on Spatiotemporal Gradients or Block Matching. *Optical Engineering*, Vol. 37, 1998, pp. 1290-1298.

[4] C.Q. Davis et al., Using a Light Microscope to measure Motions with Nanometer Accuracy, *Optical Engineering*, Vol. 37, 1998, 1299-1304.

[5] M. Hart et al., Stroboscopic Interferometer System for Dynamic MEMS Characterization, *J. of Microelectro-mechanical Systems*, Vol. 9, 2000, pp. 409 - 418.

[6] C. Rembe et al., Stroboscopic Interferometer with Variable Magnification to Measure Dynamics in an Adaptive-Optics Micromirror, *IEEE Int. Conf. on Optical MEMS 2000*, Sheraton Kauai, August 21-24, 2000, pp. 73-74.

[7] MSV 300 – Micro Scanning Vibrometer, Polytec PI product information, Tustin, California.

[8] R.A. Lawton et al., MEMS Characterization Using Scanning Laser Vibrometer, *SPIE 1999 Symposium on Microelectronic Manufacturing*, 1999.

[9] http://www.umech.com

[10] K.R. Castleman, Digital Image Processing, Printice Hall, Upper Saddle River, 1996.

[11] E. Walter et al., Identification of Parametric Models, Springer, London, 1997.

[12] J. Nelder et al., A Simplex Method for Function Minimization, *Computer Journal*, Vol. 7,1964, pp. 308-313.

[13] L. Muller, Gimballed Electrostatic Microactuators with Embedded Interconnects, Ph.D. Thesis, Dep. of Mechanical Engineering, University of California, Berkeley, 2000.

[14] L.-S. Fan et al., Batched-Fabricated Area-Efficient Milli-Actuators, *Solid State Sensor and Actuator Workshop (Hilton Head '94)*, Hilton Head, South Carolina, June 1994, pp. 38-42.

[15] L. Muller et al., Electrical Isolation Process for Molded High-Aspect-Ratio Polysilicon Microstructures, *13th Int. Workshop on Micro Electro Mechanical Systems (MEMS 2000)*, Miyazaki, Japan, January 2000, pp. 590-595.

[16] D.A. Horsley, Microfabricated Electrostatic Actuators for Magnetic Disk Drives, Ph.D. Thesis, Department of Mechanical Engineering, University of California, Berkeley, 1998.